



## 24 1 Introduction

25 The Earth's radiation belts (ERB) consist mainly of charged particles with energy from  $E \sim 100$   
26 keV to several hundreds of megaelectronvolt (MeV). In the field of the geomagnetic trap, each  
27 particles of the ERB with energy  $E$  and equatorial pitch-angle  $\alpha_0$  ( $\alpha$  is the angle between the local  
28 vector of the magnetic field and the vector of a particle velocity) makes three periodic movements:  
29 Larmor rotation, oscillations along the magnetic field line, and drift around the Earth (Alfvén and  
30 Fälthammar, 1963; Northrop, 1963).

31 Three adiabatic invariants ( $\mu$ ,  $K$ ,  $\Phi$ ) correspond to these periodic motions of trapped particles,  
32 as well as three periods of time or three frequencies: a cyclotron frequency  $f_c$ , a frequency of  
33 particle oscillations along the magnetic field line  $f_b$ , and a drift frequency of particles around the  
34 Earth  $f_d$ . For the near-equatorial ERB protons, ~~these frequencies belong to the following ranges we~~  
35 ~~have:~~  $f_c \sim 1\text{--}500$  Hz,  $f_b \sim 0.02\text{--}2$  Hz and  $f_d \sim 0.1\text{--}20$  mHz. The frequency  $f_c$  increases by tens to  
36 hundreds of times with the distance of the particle from the plane of the geomagnetic equator (in  
37 proportion to the local induction of the magnetic field), and the frequency  $f_b$  decreases by almost 2  
38 times with increasing ~~the~~ amplitude of particles oscillations.

39 ~~The frequency  $f_c$  is different for different  $L$ -shells (near the equatorial plane) and as  $L$  increases~~  
40 ~~it refers to an insignificant number of particles at higher and higher geomagnetic latitudes. Each~~  
41 ~~given value of the frequency  $f_b$  with increasing  $L$  correspond to particles of more and more higher~~  
42 ~~energies ( $E \propto L^2$ ) and its value encompass fewer and fewer particles.~~

43 ~~The number of particles with a given frequency  $f_c$  decreases rapidly with an increase of  $L$ , and~~  
44 ~~refers to higher and higher geomagnetic latitudes. For each given frequency  $f_b$ , particles become~~  
45 ~~more and more energetic with an increase of  $L$  ( $E \propto L^2$ ) and their number becomes smaller.~~

46 Compared to the frequencies  $f_c$  and  $f_b$ , the drift frequency  $f_d$  ~~of the ERB particles of~~ for one  
47 ~~particle~~ species ~~belongs to~~ has a much narrower range of values; ~~the frequency  $f_d$~~  it does not  
48 depend on the mass of ~~the~~ particles and it very weakly depends on the amplitude of their  
49 oscillations (vary within  $\sim 20\%$ ); ~~in this case, Herein,~~ on each  $L$ -shell ~~of the ERB~~ there are a  
50 significant number of particles corresponding to a certain value of  $f_d$  ~~from a narrow frequency~~  
51 ~~range.~~

52 Therefore, it can be expected that the distributions of the ERB particles in the space  $\{f_d, L\}$  will  
53 have a more ~~orderly regular~~ shape than in the space  $\{E, L\}$ , and the main physical processes in ~~the~~  
54 ~~ERB these belts~~ will manifest themselves more clearly in these distributions. ~~Furthermore,~~ it can  
55 also be expected that on these more ordered background ~~will reveal~~ more fine features ~~of the ERB~~  
56 ~~can be revealed that do would~~ not appear in the space  $\{E, L\}$ .

57 ~~Meanwhile, despite~~ Despite the importance of the drift frequency  $f_d$  for the mechanisms of the  
58 ERB formation, reliable and sufficiently complete distributions of ~~the ERB~~ particles in the ERBs  
59 (over the frequency  $f_d$ ) have not been presented ~~and these distributions have not been nor~~ analyzed;  
60 ~~indeed,~~ this is the first time. ~~This is the first time this is done here.~~

61 ~~For greater reliance, this~~ The analysis presented in this paper is limited ~~here~~ to the protons of  
62 the ERB ~~and it is refer to the~~ during magnetically quiet periods of observations ( $K_p < 2$ ), when the  
63 proton fluxes ~~of the ERB protons~~ and their spatial-energy distributions were quasi-stationary. In  
64 the following sections, the distributions of the ERB protons over their drift frequency  $f_d$  ~~were are~~  
65 constructed ~~by the~~ from experimental data (Sect. 2), and ~~these distributions were~~ analyzed (Sect.  
66 3). ~~Finally, the~~ The main conclusions of this work are given in Sect. 4.

## 67 2 Constructing the distributions of the ERB protons over their drift frequency

68 The problem of methodical differences in measurements of the fluxes of protons of the radiation  
69 belts on different satellites was one of the main ones in this work. From the published  
70 experimental data, one selected those that are in good agreement with each other and exclude from  
71 consideration all unreliable measurement results (with admixture of electrons and various ionic  
72 components of the ERB to the protons). Then, these reliable experimental results for proton fluxes  
73 and their anisotropy near the equatorial plane were represent in the space  $\{E, L\}$ ; this space is very  
74 efficient with respect to organizing experimental data obtained in different ranges of  $E$  and  $L$ .

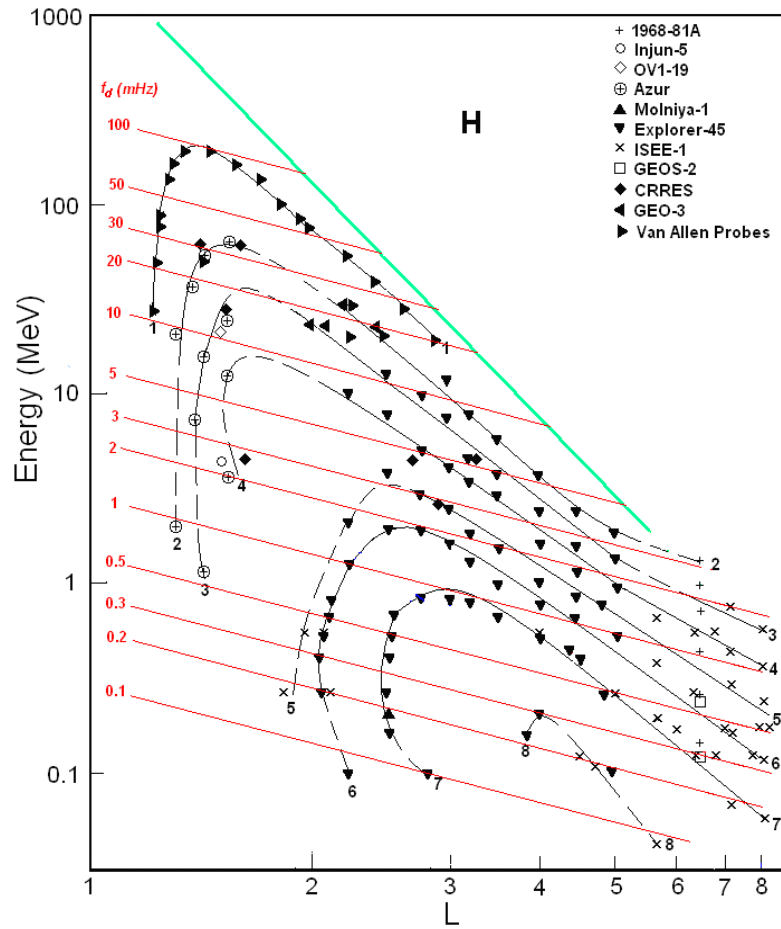
75 In such representation of experimental data, there is no need for interpolation and extrapolation  
76 of fluxes on the energy (in other representations, such necessity arises due to differences in  
77 channel widths and their positions on the energy scale for instruments installed on different  
78 satellites). In addition, with such a representation, in one figure, the data of various experiments, it  
79 is possible to construct the isolines of fluxes (and anisotropy of fluxes); these isolines cannot  
80 intersect with each other and, thus, allow to exclude a data that sharply fall out of the general  
81 picture (for more details see in Kovtyukh, 2020).

## 82 **2.1 Spatial-energy distributions of the ERB protons near the equatorial plane**

83 To construct the distributions of the ERB particles over the drift frequency, it is necessary to have  
84 reliable distributions of the differential fluxes of the ERB protons in the space  $\{E, L\}$ , where  $E$  is  
85 the kinetic energy of protons and  $L$  is the drift shell parameter.

86 ~~According to~~ From the data of ~~generalized and~~ averaged satellite measurements of the  
87 differential fluxes of protons with an equatorial pitch-angle  $\alpha_0 \approx 90^\circ$ , ~~such~~ aforementioned  
88 distributions ~~of proton fluxes for quiet conditions is~~ are constructed in (Kovtyukh, 2020) during  
89 quiet periods ( $K_p < 2$ ) near solar activity maximum in 20th (1968–1971), 22th (1990–1991), 23th  
90 (2000), and 24th (2012–2017) solar cycles. Such distributions, separately for ~~the periods near~~  
91 minima and ~~near~~ maxima of the 11-year ~~cycles of~~ solar activity cycles, ~~is~~ are constructed from ~~the~~  
92 satellite data also for other ~~main~~ ionic components of the ERB (near the equatorial plane) ~~of the~~  
93 ~~geomagnetic equator~~, but the most reliable and detailed picture was obtained in for ~~a~~ protons (see  
94 Kovtyukh, 2020).

95 In Fig. 1 one of these distributions is reproduced for periods near solar maxima ~~of the solar~~  
96 ~~activity~~ (on the data from 1968 to 2017); ~~here, Data~~ data of different satellites are associated in  
97 ~~Fig. 1~~ with different symbols. The numbers on the curves (isolines) refers to the values of the  
98 decimal logarithms of the differential fluxes  $J$  ( $\text{cm}^2 \text{ s sr MeV}^{-1}$ ) of protons (with equatorial pitch-  
99 angle  $\alpha_0 \approx 90^\circ$ ). The red lines ~~in Fig. 1~~ corresponds to the dependences  $f_d(\text{mHz}) = 0.379 \cdot L \cdot E(\text{MeV})$   
100 for the drift frequency of the near-equatorial protons in the dipole approximation of the  
101 geomagnetic field.



102

103 **Figure 1.** Distribution of the differential fluxes  $J$  in the space  $\{E, L\}$  for protons with  $\alpha_0 \approx 90^\circ$  near maxima of the  
 104 solar activity (from Kovtyukh, 2020). Data of satellites are associated with different symbols. The numbers on the  
 105 curves refers to the values of the decimal logarithms of  $J$ . Fluxes is given in units of  $(\text{cm}^2 \text{ sr MeV})^{-1}$ . The red lines  
 106 corresponds to the drift frequency  $f_d$ (mHz). The green line corresponds to the maximum energy of the trapped protons.

107 During quiet periods considered in this work, the geomagnetic field at  $L < 5-5.5$  is close to the  
 108 dipole configuration and  $L \approx L^*$ . At large  $L$ , the magnetic field differs from the dipole one even in  
 109 quiet periods; it leads to the flattening of the isolines of the proton fluxes at  $L > 5$  in Fig. 1.

110 ~~On the drift shells can be trapped only~~ Only protons with energies less than some maximum  
 111 values, determined by the Alfvén's criterion:  $\rho_c(L, E) \ll \rho_B(L)$ , where  $\rho_c$  is the gyroradius of  
 112 protons, and  $\rho_B$  is the radius of curvature of the magnetic field (near the equatorial plane) can be  
 113 trapped on the drift shells. According to this criterion and to the theory of stochastic motion of  
 114 particles, the geomagnetic trap in the dipolar region can capture and durably hold only protons  
 115 with  $E$  (MeV)  $< 2000 \cdot L^{-4}$  (Ilyin et al., 1984). The green line in Fig. 1 represents this boundary.

116 The distribution of the ERB proton fluxes shown in Fig. 1, refers to the years of the solar  
 117 maximum, but the solar-cyclic variations in the ERB proton fluxes are small and localized at  $L <$   
 118 2.5 (mainly at  $L < 1.4$ ) (see Kovtyukh, 2020).

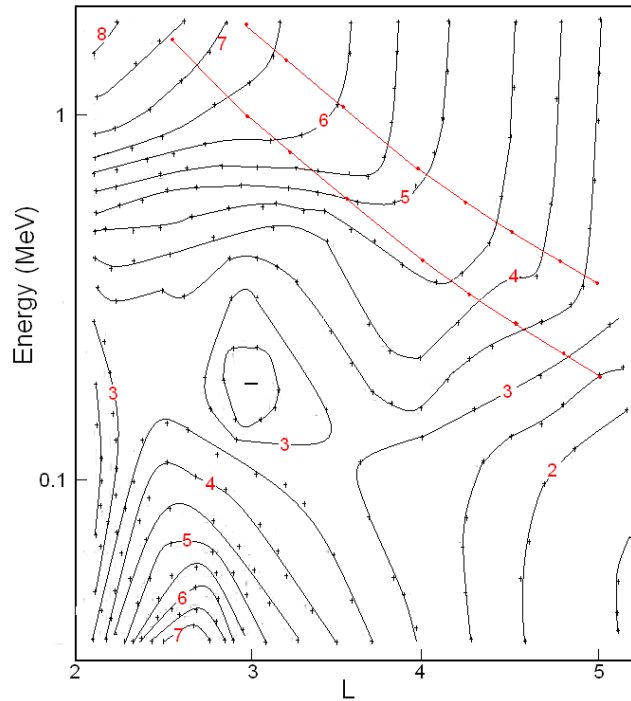
## 119 2.2 Spatial-energy distributions of the ERB protons outside the equatorial plane

120 The quasi-stationary fluxes  $J$  of the ERB particles with given energy and local pitch-angle  $\alpha$   
 121 decrease usually when the point of observation is shifted from the equatorial plane to higher  
 122 latitudes along a certain magnetic field line. In the inner regions of the ERB, on  $L < 5$ , an angular  
 123 distributions of protons have usually a maximum at the local pitch-angle  $\alpha = 90^\circ$ . In wide interval  
 124 near this maximum these distributions are well described by the function

125  $J(\alpha, B/B_0) \propto (B/B_0)^{-A/2} \sin^A \alpha$  (Parker, 1957), where  $A$  is the index of an anisotropy of a  
 126 fluxes,  $B$  is the induction of a magnetic field at the point of measurements of these fluxes and  $B_0$  is  
 127 induction of a magnetic field at the equatorial plane on the same magnetic line.

128 ~~On the data of the satellites Van Allen Probes, on  $L > 4.5$  pitch angle distributions of proton~~  
 129 ~~fluxes at  $E \sim 0.05 - 0.5$  MeV strongly depend on MLT (Shi et al., 2016). The average index  $A$~~   
 130 ~~values on the day side are larger than on the night side, and this dependence becomes more distinct~~  
 131 ~~with increasing energy. These results indicate that drift shell splitting play an important role in the~~  
 132 ~~formation of these distributions at  $L > 4.5$ .~~

133 The **generalized** empirical model of an anisotropy  $A(E, L)$  for the proton fluxes with  $E \sim 0.1-2$   
 134 MeV on  $L \sim 2-5$  near the equatorial plane for the **quasi-stationary** ERB (for quiet periods with  $Kp$   
 135  $< 2$ ) is presented in Fig. 2. The anisotropy index  $A$  of ~~the proton~~ these fluxes is shown in Fig. 2, in  
 136 the space  $\{E, L\}$ , in the form of isolines with the same values  $A$  from 1.5 to 8.0 and with a step  $\Delta A$   
 137  $= 0.5$ . The integer values of this index are plotted on the corresponding isolines ~~in~~ as red numbers.



138

139 **Figure 2.** Empirical model of the anisotropy index  $A(E, L)$  of the ERB proton fluxes averaged on the data of the  
 140 satellites obtained near the plane of the geomagnetic equator. Values of  $A$  are given on isolines of the anisotropy:  $A =$   
 141  $1.5-8.5$  with the step  $\Delta A = 0.5$ .

142 When constructing this model, we consider and analyze the data of the following satellites:  
 143 Explorer-12 (Hoffman and Bracken, 1965), Explorer-14 (Davis, 1965), Explorer-26 (Søraas and  
 144 Davis, 1968), OV1-14 and OV1-19 (Fennell et al., 1974), Explorer-45 (Williams and Lyons, 1974;  
 145 Fritz and Spjeldvik, 1981; Garcia and Spjeldvik, 1985), ISEE-1 (Garcia and Spjeldvik, 1985;  
 146 Williams and Frank, 1984), SCATHA (Blake and Fennell, 1981), Van Allen Probes (Shi et al.,  
 147 2016), and other satellites. These data were obtained in 1961-2015.

148 ~~Figure 2~~ Fig. 2 shows that for rather high energy ( $> 1$  MeV) the anisotropy of a proton fluxes  
 149 monotonically increases with decreasing  $L$  (from  $A \sim 3.5$  to  $A \sim 8.0$ ). For  $E > 0.3$  MeV on  $L < 3$   
 150 anisotropy is monotonically increases with increasing energy, but for  $E > 0.5$  MeV on  $L > 3$  it is  
 151 almost **energy-independent** ~~on-energy~~.

152 Some small irregularities of the isolines in Fig. 2 are ~~connect~~ **due** to the fact that experimental  
 153 data were used for constructing this figure; ~~these data~~ were obtained in different years, with  
 154 different instruments ~~on different orbits of satellites~~, and during different intensity of the solar

155 activity. At the same time, Fig. 2 demonstrates the important regularities of the pitch-angle  
 156 distributions of the **quasi-stationary ERB protons fluxes**.

157 In the region  $\{E > 0.5 \text{ MeV}, L > 3\}$  the isolines of the anisotropy index are almost parallel to  
 158 each other and to the energy **scale axis**. This adiabatic regularity refers **for** to protons belonging to  
 159 the power-law tail of their energy spectra, the exponent of which practically does not change when  
 160  $L$  changes (at  $L > 3$ ). In Fig. 2, the red lines correspond to the lower boundary of the power-law tail  
 161 of the ERB protons energy spectra:  $E_b = (36 \pm 11) L^{-3} \text{ MeV}$  (see Kovtyukh, 2001, 2020).

162 The pattern of  $A(E, L)$  in the region on  $L > 3$  at  $E \sim 0.2\text{--}0.5 \text{ MeV}$  and the local minimum at  $L \sim$   
 163  $3$  ( $E \sim 0.2 \text{ MeV}$ ) are connected with local maximum in the **quasi-stationary proton energy spectra**  
 164 of the ERB which corresponds to  $E = (17 \pm 3) L^{-3} \text{ MeV}$  (see Kovtyukh, 2001, 2020).

165 These regularities in the pattern of  $A(E, L)$  are explained within the framework of the theory of  
 166 radial transport (diffusion) of the ERB protons with conservation of the adiabatic invariants  $\mu$  and  
 167  $K$  of their periodic motions (these **questions issues** were most fully considered in Kovtyukh, 1993).

168 ~~Local~~ **Both the local** maximum at  $L \sim 2.5$  ( $E < 0.1 \text{ MeV}$ ) and the region of low anisotropy at  $L \sim$   
 169  $2$  ( $E \sim 0.1 \text{ MeV}$ ) in Fig. 2, are **connected with related to** the ionization losses of protons.

170 **On the data of the satellites, the pitch-angle distributions of the ERB proton fluxes strongly**  
 171 **depend on MLT at  $L > 5$ :** the average index  $A$  values on the day side are larger than on the night  
 172 side, and this dependence becomes more distinct with increasing energy (see, e.g., Shi et al., 2016).  
 173 These results indicate that drift shells splitting (Roederer, 1970) play an important role in the  
 174 formation of these distributions at  $L > 5$ . **In the calculations performed here, it was assumed that**  
 175 **near the equatorial plane the pitch-angle distributions of the ERB proton fluxes at  $L > 6$ , averaged**  
 176 **over MLT, at  $\alpha_0 \sim 90^\circ$  are nearly isotropic.**

177 High anisotropy for the fluxes of protons at  $E = 5\text{--}50 \text{ MeV}$  and a strong dependence  $A(L)$  at the  
 178 inner boundary of the inner belt ( $L = 1.15\text{--}1.40$ ,  $B/B_0 = 1.0\text{--}1.7$ ) were obtained on the satellite  
 179 DIAL (Fischer et al., 1977). According to these data, an anisotropy index increase from  $A \sim 12$  at  
 180  $L = 1.25$  to  $A \sim 60$  at  $L = 1.15$ , and do not depends on  $L$  at  $L = 1.25\text{--}1.40$ . These results are supported  
 181 by the data of the satellite Resurs-01-N4 for the protons with  $E = 12\text{--}15 \text{ MeV}$  which **were** obtained  
 182 at  $h \sim 800 \text{ km}$  (Leonov et al., 2005). They will be taken into account in our calculations.

183 The experimental results on the pitch-angle distributions of the ERB proton fluxes and their  
 184 anisotropy indexes were discussed in detail in (Kovtyukh, 2018).

## 185 **2.3 Drift frequency distributions of the ERB protons**

186 Based on the results shown in Fig. 1 and 2, one can calculate the distributions of the ERB protons  
 187 over the drift frequency  $f_d$ . In these calculations, the dipole model of the geomagnetic field was  
 188 used, according to which (see, e.g., Roederer, 1970) the point of the magnetic field line at **a given**  
 189  **$L$  and a geomagnetic latitude  $\lambda$**  is located from the center of the dipole at a distance

$$190 \quad R(L, \lambda) = R_E L \cos^2 \lambda,$$

191 where  $R_E$  is the Earth's radius, and the field induction at a given  $L$  changes with changing  $\lambda$  as

$$192 \quad B(L, \lambda) = \frac{\sqrt{4 - 3 \cos^2 \lambda}}{\cos^6 \lambda} B_0(L),$$

193 where  $B_0(L) = 0.311 \text{ Gs} \times L^{-3}$ .

194 It was also taken into account that the drift frequency  $f_d$  of the nonrelativistic particles depends  
 195 essentially only on their kinetic energy  $E$  and on  $L$ . This value depends very slightly on the particle  
 196 pitch-angle: with an increase in the geomagnetic latitude of the mirror point of the particle trajectory  
 197 from  $0$  to  $10^\circ$ , it increases by only  $1.5\%$ ; and in the range from  $0$  to  $20\text{--}30^\circ$  it increases by  $5.8\text{--}12.5\%$ .

198 The number of protons with energies from  $E$  to  $E+dE$  per unit volume  $n$  is equal to the differential  
 199 flux of these particles  $J$  (falling per unit time per unit area of the detector per unit solid angle), divided  
 200 by the velocity  $v$  of these particles:  $n = J/v$ . For nonrelativistic protons with mass  $m$ , this velocity is  
 201  $(2E/m)^{1/2}$ .

202 Then in the near-equatorial region, between  $L$  and  $L+dL$  and within geomagnetic latitudes from  
 203 0 to  $\pm\lambda_0$ , the total number of nonrelativistic protons with mirror points within this region and with  
 204 energy from  $E$  to  $E+dE$ , drifting on a given  $L$  with frequency  $f_d(L,E)$  around the Earth, is

$$\Delta N(L, f_d) = 2 \int_0^{\lambda_0} 2\pi R_E^2 L dL \frac{B_0(L)}{B(L, \lambda)} R_E L \cos \lambda \sqrt{4 - 3 \cos^2 \lambda} d\lambda \times$$

$$4\pi \int_{\alpha_{01}}^{\alpha_{02}} \frac{J(L, E(L, f_d)) dE}{\sqrt{2E(L, f_d)/m}} \sin^A \alpha_0 \cos \alpha_0 d\alpha_0$$

206 where  $m$  is the rest mass of a proton,  $J(L, E(L, f_d))$  is the differential fluxes and  $E(L, f_d)$  is the  
 207 protons energy. The first integral takes into account that the magnetic flux in the layer between  
 208 shells  $L$  and  $L+dL$  it conserved when latitude  $\lambda$  changes, i.e.

$$2\pi R_E L \cos \lambda R_E dL = 2\pi R_E L \frac{B_0(L)}{B(L, \lambda)} R_E dL.$$

210 As result of integrating the last expression over  $\alpha_0$  and replacing  $\cos \lambda \equiv t$ , we obtain:

$$\Delta N(L, f_d) = 4\pi R_E^3 L^2 dL \frac{J(L, E(L, f_d)) dE}{\sqrt{2E(L, f_d)/m}} \times \frac{4\pi}{A+1} \times$$

$$\int_{\cos \lambda_0}^1 t^7 \left[ \left( \frac{t^6}{\sqrt{4-3t^2}} \right)^{\frac{A+1}{2}} - (0.565)^{A+1} \right] dt$$

212 When integrating over equatorial pitch-angles  $\alpha_0$ , Liouville's theorem and the conservation of  
 213 the first adiabatic invariant ( $\mu$ ) are taken into account:  $\sin^2 \alpha_{01} = B_0(L)/B(L, \lambda_0)$  and  $\sin^2 \alpha_{02} =$   
 214  $B_0(L)/B(L, \lambda)$ , where  $B(L, 0) = B_0(L)$ .

215 With an increase  $\lambda$  from 0 to  $\lambda_0 = 30^\circ$ , the value of the function  $\sqrt{4-3t^2}$  increases from 1 to  
 216 1.32, i.e. deviates from the average value (1.16) by only 16%. Most part of the ERB protons are  
 217 concentrated at these latitudes. Therefore, when calculating the last integral, we will assume that

$$\sqrt{4-3t^2} \approx 1.16.$$

219 Then you can get the following expression:

$$\Delta N(L, f_d) = k \frac{J(L, E(L, f_d))}{\sqrt{E(L, f_d)}} F(A) L^2 dL dE,$$

221 where

$$F(A) = \frac{1}{A+1} \left[ \frac{(1.16)^{-(A+1)/2}}{3A+11} (1 - 0.21 \cdot 0.65^A) - 0.085 (0.565)^{A+1} \right]$$

224 and

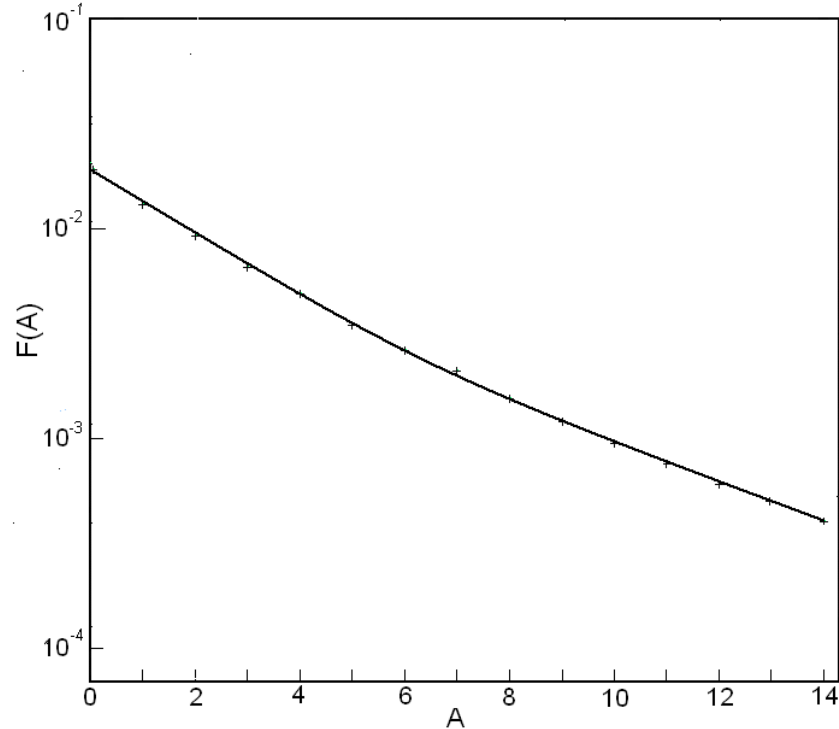
$$k = (4\pi)^2 R_E^3 \sqrt{m/2} = 2.945 \cdot 10^{19} \text{ cm}^2 \text{ s sr MeV}^{1/2}.$$

225

226 When calculating the values of  $\Delta N$ , we will take that  $dL/L = dE/E = 0.1$ . Finally, for the  
 227 indicated ERB region near the equatorial plane, we obtain:

$$228 \quad \Delta N(L, f_d) = 2.945 \cdot 10^{17} J(L, E(L, f_d)) \sqrt{E(L, f_d)} F(A) L^3, \quad (1)$$

229 where  $J$ , the differential fluxes of protons with equatorially pitch-angle  $\alpha_0 \approx 90^\circ$ , is given in units  
 230 of  $(\text{cm}^2 \text{ s sr MeV})^{-1}$ , and the energy of protons  $E$  is given in MeV. The dependence  $F(A)$  is shown  
 231 in Fig. 3.

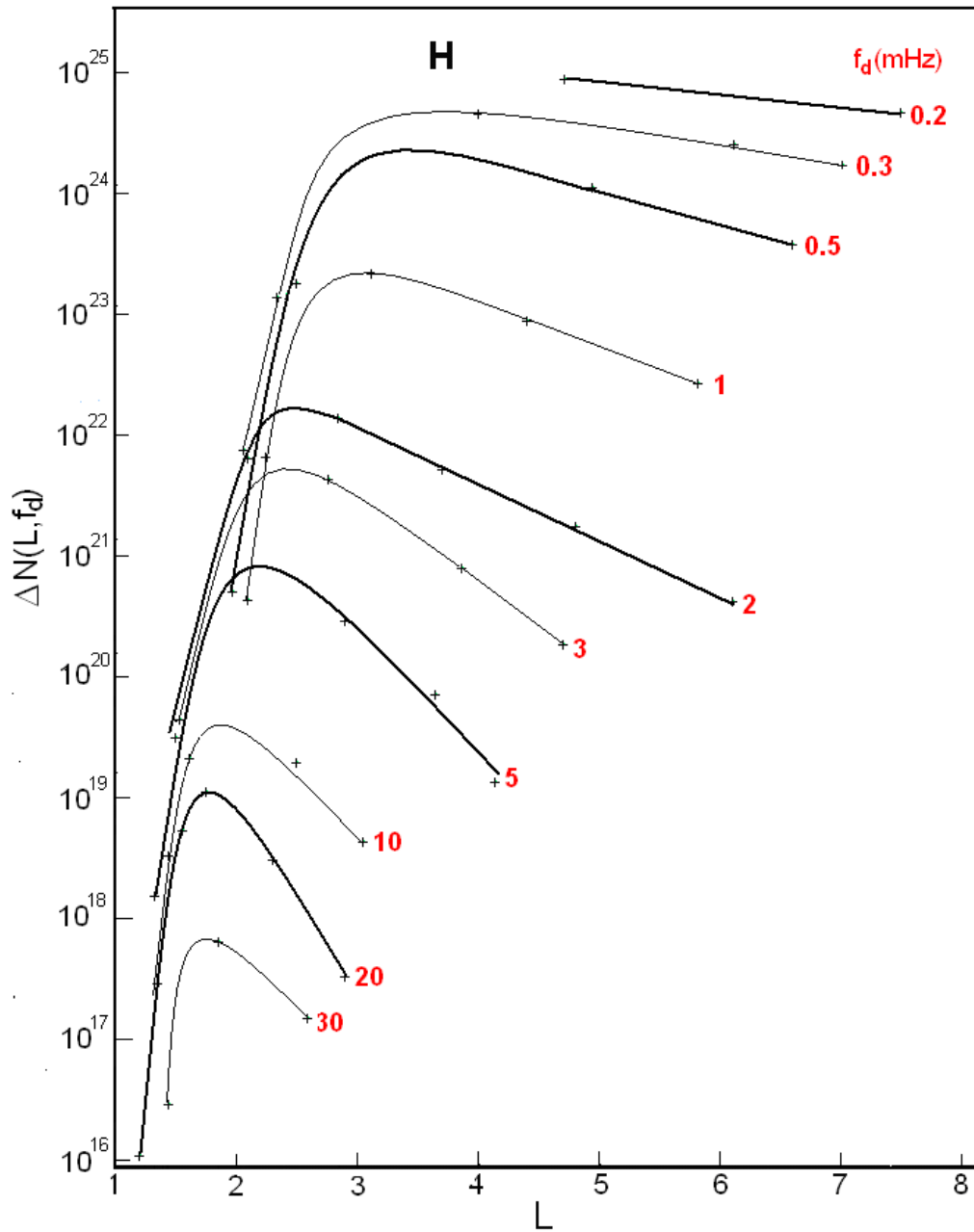


232

233 **Figure 3.** Dependence of the factor  $F(A)$  in formula (1) on the anisotropy index  $A$  of the proton fluxes.

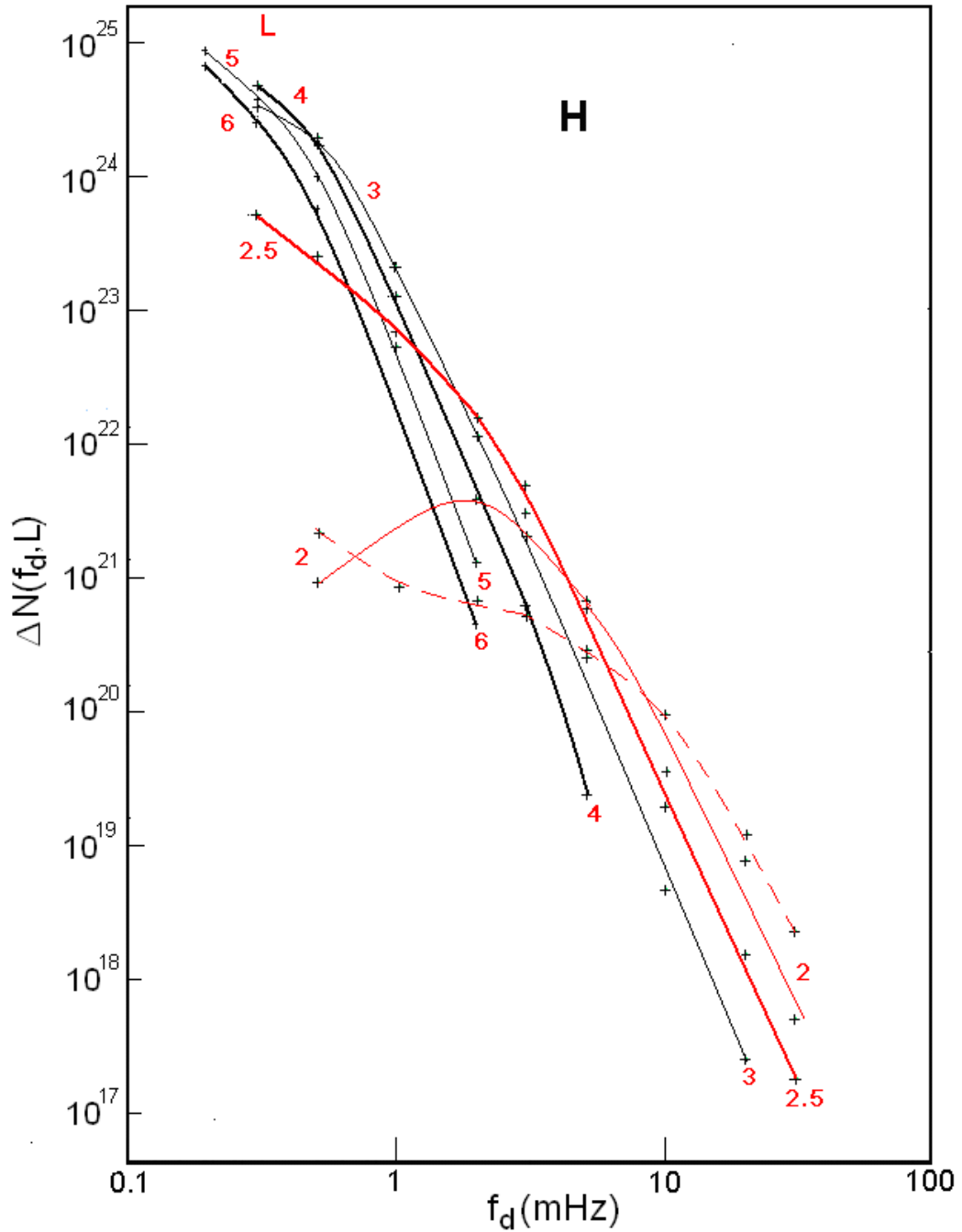
234 For protons of the ERB, the radial profiles  $\Delta N(L, f_d)$  for  $f_d = 0.2, 0.3, 0.5, 1, 2, 3, 5, 10, 20,$  and  
 235 30 mHz, calculated by using the formula (1) together with using Figs. 1–3 are shown in Fig. 4, and  
 236 the frequency spectra  $\Delta N(f_d, L)$  at  $L = 2, 2.5, 3, 4, 5,$  and 6 are shown in Fig. 5. Near each curve in  
 237 Fig. 4, the corresponding value of  $f_d$ (mHz) is indicated, and each spectrum in Fig. 5 have the  
 238 corresponding  $L$  value (these values are highlighted in red). For clarity, in Figs. 4 and 5, thin  
 239 curves alternate with thick curves and in Fig. 5 spectra at  $L = 2$  and 2.5 are highlighted in red.





240

241 **Figure 4.** Radial profiles  $\Delta N(L, f_d)$  for protons of the ERB with drift frequencies  $f_d = 0.2, 0.3, 0.5, 1, 2, 3, 5, 10, 20$  and  
 242 30 mHz, plotted for periods of **maximum** solar activity **maxima**. The  $f_d$  values corresponding to each curve are  
 243 highlighted in red. For clarity, thin curves are interspersed with thick curves.



244  
245  
246  
247  
248  
249

**Figure 5.** Frequency spectra  $\Delta N(f_d, L)$  for protons of the ERB at  $L = 2, 2.5, 3, 4, 5$  and  $6$ , plotted for periods of maximum solar activity maxima. The values  $L$  corresponding to each spectrum and spectra at  $L = 2$  and  $2.5$  are highlighted in red. The red dotted line shows the spectrum  $\Delta N(f_d, L)$  of the ERB protons at  $L = 2$ , constructed from data for during minimum periods of solar activity minima (see Kovtyukh, 2020). For clarity, thin curves are interspersed with thick curves.

250  
251  
252

The errors of these calculations consist mainly of the errors of the averaged experimental data shown in Figs. 1 and 2 (these errors are most significant at  $L < 2$ ), and because of the deviations of the geomagnetic field from the dipole model at  $L > 5$ .

253  
254  
255  
256  
257

As  $\lambda_0$  decreases, the errors in our calculations will decrease. These errors can be reduced also by using numerical computer calculations. However, it should be taken into account that even in very quiet periods of observations the fluxes of the ERB protons, as well as the energy spectra and pitch-angle distributions of these fluxes, may experience changes that exceed the errors of our calculations ~~even in very quiet periods of observations~~.

259 In agreement with the results of experimental and theoretical studies, at  $L > 2$ , the main mechanism  
 260 for the formation of the ERB ~~for~~ protons is the radial diffusion of particles from the outer boundary  
 261 of the geomagnetic trap to the Earth under conservation the adiabatic invariants  $\mu$  and  $K$  (see, e.g.,  
 262 Lejosne and Kollmann, 2020; Kovtyukh, 2016b, 2018).

263 ~~Figures~~ Figs. 1 and 2 presented here make it possible to determine ~~in which the~~ regions of the  
 264  $\{E, L\}$  space near the equatorial plane ~~in which~~ the ionization losses of ions during their radial  
 265 diffusion can be neglected and where they cannot.

266 The isolines of ~~the~~ proton fluxes in Fig. 1 at sufficiently large  $E$  and  $L$  go up with decreasing  $L$ ,  
 267 in the direction of increasing energy, in strict agreement with the adiabatic laws of radial transport  
 268 of particles. At lower  $L$  these isolines ~~reject-deflect to the low energies~~ do change the direction of  
 269 ~~their course~~, under the influence of ionization losses, which increase rapidly with decreasing  $L$  (see  
 270 in Kovtyukh, 2020 for details).

271 At sufficiently large values of  $E$  and  $L$ , isolines of the anisotropy index in Fig. 2 pass practically  
 272 parallel to each other and parallel to the energy axis, in agreement with the laws of adiabatic  
 273 transport of particles with power-law energy spectra (see Kovtyukh, 1993). At lower  $E$  and  $L$ , a  
 274 more complex picture is formed under the influence of ionization losses (for more details see in  
 275 Kovtyukh, 2001, 2018).

276 With decreasing  $L$ , the radial diffusion ~~are~~ is decreased very rapidly, and the belt of protons  
 277 with  $E > 10\text{--}20$  MeV on  $L < 2$  is generated mainly as result of decay a neutrons of albedo which  
 278 are knocked from the atmospheric atoms nuclei by the Galactic Cosmic Rays (GCR) protons. This  
 279 mechanism (CRAND) is simulated in many contemporary studies based on the experimental data  
 280 (see, e.g., Selesnick et al., 2007, 2013, 2014, 2018).

281 The mechanisms of formation of the ERB under the action of radial diffusion and CRAND are  
 282 manifested and clearly differ both in the radial profiles  $\Delta N(L, f_d)$  and in the frequency spectra  
 283  $\Delta N(f_d, L)$  of protons.

284 Let us consider the manifestations of these mechanisms in Fig. 4 and 5 and related effects.

285 In contrast to the radial profiles of fluxes  $J(L, E)$ , the radial profiles  $\Delta N(L, f_d)$  for protons with  $f_d$   
 286  $< 5$  mHz (see Fig. 4) have much less steeper ~~of the~~ outer edges and their steepness decreases with  
 287 decreasing frequency  $f_d$ . This effect is connected mainly with an increase in the volume of  
 288 magnetic tubes (factor  $L^3$  in formula (1) from Section 2.3) and with a decrease in the anisotropy  
 289 index of proton fluxes with increasing  $L$ .

290 At the same time, in comparison with the radial profiles  $J(L, E)$ , the radial profiles  $\Delta N(L, f_d)$   
 291 have more steeper inner edges. This effect is ~~mainly~~ connected ~~mainly with~~ to the large anisotropy  
 292 of proton fluxes in the corresponding region of space  $\{E, L\}$  and with the rapid growth of the  
 293 anisotropy index with decreasing  $L$  in this region. It is especially expressed in the radial profiles  
 294  $\Delta N(L, f_d)$  at  $f_d \sim 0.3\text{--}1$  mHz (see Fig. 4); this is due to the fact that in the corresponding region of  
 295 space  $\{E, L\}$  the anisotropy index of proton fluxes strongly depends on  $E$  and  $L$  (see Fig. 2).

296 Radial profiles  $\Delta N(L, f_d)$  at  $f_d > 10$  mHz are formed by the mechanism CRAND. They have a  
 297 maximum at  $L \sim 1.5\text{--}2.0$ , and the steepness of their inner and outer edges does not differ as much  
 298 as for lower frequencies  $f_d$  (see Fig. 4). When constructing these profiles, it was taken into account  
 299 that at  $E = 5\text{--}50$  MeV an anisotropy index  $A$  of proton fluxes do not depend on  $L$  at  $L = 1.25\text{--}1.40$ :  
 300  $A = 12 \pm 2$  (Fischer et al., 1977; Leonov et al., 2005).

301 The shape of the spectra  $\Delta N(f_d, L)$  at  $L > 3$  is determined, first of all, by the shape of the energy  
 302 spectra of proton fluxes  $J(E, L)$  at the outer boundary of the geomagnetic trap. Gradually, as the  
 303 particles diffuse to the Earth, their energy spectra are transformed under the action of betatron  
 304 acceleration and ionization losses of particles.

305 In contrast to the energy spectra of proton fluxes  $J(E, L)$ , distributions  $\Delta N(f_d, L)$  of the ERB  
 306 protons over their drift frequency  $f_d$  (Fig. 5) differ much less from each other at  $L > 3$ . Such  
 307 convergence of the spectra  $\Delta N(f_d, L)$  is driven by increase in the volume of magnetic tubes and a  
 308 decrease in the anisotropy index of the ERB proton fluxes with increasing  $L$ . ~~Figure 5 testify for~~  
 309 ~~close~~ Fig. 5 demonstrates the closeness to the adiabatic transformations of the spectra  $\Delta N(f_d, L)$   
 310 when  $L$  changes at  $L > 3$ .

311 The energy spectra of near-equatorial proton fluxes  $J(E, L)$  with  $E > 10 \cdot L^{-3}$  MeV at  $L > 3$  in  
 312 quiet periods have a local maximum at  $E = (17 \pm 3) \cdot L^{-3}$  MeV and a power-law tail ( $J \propto E^{-\gamma}$ , where  $\gamma$   
 313  $= 4.25 \pm 0.75$ ) at  $E > (36 \pm 11) \cdot L^{-3}$  MeV (Kovtyukh, 2001, 2018, 2020).

314 The frequency spectra of the ERB protons at  $L > 3$  weakly depend on  $L$  and over the considered  
 315 range  $\Delta f_d$  have a close to power-law shape with an exponent  $\gamma = 4.71 \pm 0.43$  (at  $f_d > f_d^*$ , where  $f_d^*$   
 316  $\sim 0.5$  mHz at  $L \sim 3-6$ ,  $\sim 2$  mHz at  $L = 2.5$  and  $\sim 5$  mHz at  $L = 2$ ). Note that the spread of the  
 317 parameter  $\gamma$  for the frequency spectra of protons is almost 2 times less than for their energy spectra.  
 318 These spectra become more rigid (flattened) at  $f_d < f_d^*$ .

319 Thus, the average exponents of the power-law tail of the energy and frequency spectra of  
 320 protons differ by  $\Delta\gamma = 0.46$ , and there is no local maximum in the frequency spectra at  $f_d > 2$  mHz  
 321 at  $L > 2.5$ . The main role in such differences in the shape of the energy and frequency spectra of  
 322 protons was played by the factor  $F(A)$  in formula (1), in which the anisotropy index  $A$  is a function  
 323 of  $E$  and  $L$  (see Figs. 2 and 3). Note that in the region  $\{E > 0.5 \text{ MeV}, L > 3\}$  the anisotropy index  
 324  $A$ , as well as the protons energy, is transformed according to adiabatic laws when  $L$  changes (see  
 325 Fig. 2 and comments to it).

326 These results confirm our hypothesis about the ordering of the distributions of protons over  
 327 their drift frequency  $f_d$  in the outer regions of the ERB, at  $L > 3$ , where most of the ERB protons  
 328 are located and where the radial diffusion of protons overpowers their ionization losses.

329 At all  $L$ , the frequency spectra  $\Delta N(f_d, L)$  become more flat at small  $f_d$  (at small ~~and~~  $E$ ) under  
 330 influence ionization losses. However, in the range of high  $f_d$  (from 3–5 mHz to 30 mHz), for  
 331 protons with high energies and low ionization losses, the protons frequency spectra ~~save~~ have a  
 332 power-law tail even at  $L = 2$  (see Fig. 5).

333 For protons with  $f_d < 0.5$  mHz, which correspond to the ERB protons of the lowest energies,  
 334 ionization losses lead to the same consequences at higher  $L$ -shells: the radial profiles  $\Delta N(L, f_d)$   
 335 approach each other, and the spectra  $\Delta N(f_d, L)$  flatten out (see Figs. 4 and 5).

336 In the region of the steep inner edge of the radial distributions  $\Delta N(L, f_d)$ , spectra  $\Delta N(f_d, L)$  of the  
 337 ERB protons ~~gradually, with decreasing  $L$~~ , become ~~gradually~~ increasingly rigid ~~with decreasing  $L$~~ ,  
 338 and rapidly diverge from each other (see Fig. 4 and 5). In the range of small  $f_d$  at  $L < 2.5$ , the  
 339 connection between these distributions and the shape of the boundary energy spectra of protons is  
 340 gradually lost.

341 These results indicate a violation of the order in the distributions of protons under the influence  
 342 of ionization losses.

343 In Fig. 5, the dotted line also shows the spectrum  $\Delta N(f_d, L)$  of the ERB protons at  $L = 2$ ,  
 344 constructed from experimental data for periods of low solar activity ~~between the 19th/20th,~~  
 345 ~~20th/21th, 21th/22th, and 22th/23th solar cycles~~ (see Fig. 1 in Kovtyukh, 2020). ~~Figure Fig. 5 show~~  
 346 that at  $L = 2$  for  $f_d > 10$  mHz there were more protons at the minimum of solar activity, and for  $f_d \sim$   
 347  $1-10$  mHz there were more protons at the maximum of solar activity.

348 The effect of a decrease in the  $\Delta N(f_d, L)$  values for protons with  $f_d > 10$  mHz at  $L < 2$  with an  
 349 increase in solar activity is mainly connected with a decrease in the fluxes of protons with  $E > 10-$   
 350  $20$  MeV here. This effect is well known. It is described by the CRAND mechanism (see, e.g.,

351 Selesnick et al., 2007) and was considered in detail in (Kovtyukh, 2020). With an increase in solar  
352 activity, the densities of atmospheric atoms and ionospheric plasma on small  $L$ -shells significantly  
353 increase, which leads to an increase in ionization losses of the ERB protons, ~~but~~ and the power of  
354 their main source (CRAND) practically does not change. As a result, the equilibrium fluxes and  
355  $\Delta N(f_d, L)$  for protons with  $f_d > 10$  mHz are established at lower levels.

356 However, the effect of an increase in  $\Delta N(f_d, L)$  for  $f_d \sim 1\text{--}10$  mHz at low  $L$  with increasing solar  
357 activity, corresponding to the protons of lower energies, was discovered here for the first time.

358 With decreasing ~~in~~  $E$  (and  $f_d$ ) of protons their ionization losses increase, and if the fluxes of  
359 low-energy protons in the inner belt were also formed by the CRAND mechanism, one would have  
360 observed even stronger increase of their fluxes with ~~decreasing~~ solar activity ~~decreasing~~, than for  
361 protons with  $E > 10\text{--}20$  MeV ( $f_d > 10$  mHz). But for protons with  $f_d \sim 1\text{--}10$  mHz, we see in Fig. 5  
362 ~~reverse the opposite~~ effect in the spectra  $\Delta N(f_d, L)$  at  $L = 2$ , which is not described by the CRAND  
363 mechanism.

364 On the other hand, it was proved that quasi-stationary fluxes of protons with  $E < 15$  MeV at  $L \sim$   
365 2 are formed mainly by the mechanism of protons radial diffusion from the external region of the  
366 ERB (Selesnick et al., 2007, 2013, 2014, 2018). These fluxes and  $\Delta N(f_d, L)$  values for  $f_d \sim 1\text{--}10$   
367 mHz at  $L = 2$  are formed as a result of a balance of competing processes radial diffusion of protons  
368 and their ionization losses.

369 The rates of transport of the ERB protons to the Earth (radial diffusion) rapidly increase with  
370 decreasing particles energy (see Kovtyukh, 2016b). In addition, with an increase in solar activity,  
371 the average level of geomagnetic fluctuations in the ERB increases. Under ~~the~~ influence of these  
372 factors, one can expect a significant increase in the intensity of radial diffusion of the low-energy  
373 protons at low  $L$  with an increase in solar activity. As a result, the effect of increasing in the  
374 density of a dissipative medium with an increase in solar activity ~~is~~ overpowered by a more  
375 significant effect of increasing in the rates of radial diffusion of protons.

376 According to ~~a~~ numerous experimental data, during magnetic storms, ~~a wide variety of complex~~  
377 ~~and-varied~~ spectra of powerful pulsations of magnetic and electric fields in the ~~considered~~  
378 frequency range ~~considered here~~ (ULF) can be generate in the geomagnetic trap, which are non-  
379 regularly distributed over  $L$ ; these pulsations can lead to local acceleration and losses of the ERB  
380 particles (see, e.g., Sauvaud et al., 2013). Such effects will violate the regular characteristics of the  
381 protons distributions shown in Fig. 4 and 5. However, ~~in~~ during quiet periods ( $K_p < 2$ ), the  
382 amplitudes of such pulsations are small and they lead only to radial diffusion of particles.

## 383 4 Conclusions

384 ~~On the basis of generalized~~ From the data on ~~the fluxes of~~ near-equatorial ~~protons of the~~ ERB  
385 proton fluxes (with energy from  ~~$E \sim 0.2$  MeV~~ to 100 MeV ~~at and~~ drift  $L$  shells  ~~$L$  ranging~~ from  $\sim 1$   
386 to 8), their quasi-stationary distributions ~~of the ERB protons~~ over the drift frequency of particles  
387 around the Earth ( $f_d$ ) were constructed. The results of calculations of the number ~~of protons~~  $\Delta N$   
388 of the ERB protons within  $30^\circ$  in geomagnetic latitude at different  $L$  and  $f_d$  for periods of ~~maximum~~  
389 solar activity ~~maximum~~ are presented. They differ from the corresponding distributions of the ERB  
390 protons for periods of low solar activity only at  $L < 2.5$  (for comparison, the spectra of these  
391 distributions are given at  $L = 2$ ).

392 The radial profiles of these distributions  $\Delta N(L, f_d)$  have ~~only~~ one maximum that shifts toward  
393 the Earth with increasing  $f_d$ . In comparison to the proton fluxes profiles  $J(L, E)$ , the radial profiles  
394  $\Delta N(L, f_d)$  at  $f_d < 5$  mHz have steeper inner edges and flatter outer edges. However, the radial  
395 profiles  $\Delta N(L, f_d)$  at  $f_d > 10$  mHz, which are formed by the CRAND mechanism, have inner and  
396 outer edges with only slightly difference from each other ~~in~~ for what concerns the steepness of  
397 their profiles.

398 In contrast to the energy spectra of proton fluxes  $J(E, L)$ , the frequency spectra  $\Delta N(f_d, L)$  of the  
399 ERB protons at  $L > 3$  are weakly dependent on  $L$  and, for sufficiently large  $f_d$  they have a nearly  
400 power-law ~~form~~ shape with an exponent  $\gamma = 4.71 \pm 0.43$ . There is no local maximum in these  
401 spectra in the region  $\{f_d > 2 \text{ mHz}, L > 2.5\}$ , as in the corresponding  $J(E, L)$  spectra.

402 The main physical processes in the ERB (radial diffusion, ionization losses of particles and  
403 mechanism CRAND) manifested clearly in these distributions.

404 Distributions  $\Delta N(L, f_d)$  and  $\Delta N(f_d, L)$  of the ERB protons in the region  $\{f_d > 0.5 \text{ mHz}, L > 3\}$   
405 have a more ~~orderly form~~ regular shape than in the corresponding region of the space  $\{E, L\}$ , ~~and~~  
406 ~~the main physical processes in the ERB manifested more clearly in these distributions~~. In these  
407 regions, there is ~~most~~ the majority of the ERB protons, ~~are located~~ and their radial diffusion ~~of~~  
408 ~~protons~~ overpowers their ionization losses during the transport of particles to the Earth.

409 In the region of the steep inner edges of the radial distributions  $\Delta N(L, f_d)$ , the spectra  $\Delta N(f_d, L)$   
410 of protons rapidly diverge from each other with decreasing  $L$ , and at low frequencies these spectra  
411 become flatten. These results indicate a violation of the order in these distributions of protons  
412 under the influence of ionization losses.

413 With increasing ~~in~~ solar activity, the number of protons  $\Delta N(f_d, L)$  at  $L \sim 2$  decreases for  $f_d > 10$   
414 mHz and increases for  $f_d \sim 1\text{--}10$  mHz. The effect at high  $f_d$ , corresponding to protons with  $E > 15$   
415 MeV, is well known and is described in the framework of the CRAND mechanism.

416 However, the opposite effect at low  $f_d$ , corresponding to the lower-energy protons, is discovered  
417 here for the first time. This effect can be associated with the fact that the low-frequency part of the  
418 spectrum  $\Delta N(f_d, L)$  of protons, even at  $L \sim 2$ , is ~~mainly~~ formed ~~mainly~~ by the mechanism of  
419 protons transport from the outer regions of the ERB. This effect may indicate that with increasing  
420 ~~of the~~ solar activity, the average rates of radial diffusion of protons increase ~~also~~ as well. For low-  
421 energy protons at  $L \sim 2$ , the effect of increasing density of a dissipative medium with increasing  
422 solar activity is overpowered by ~~the increasing~~ increase of the rates of radial diffusion of particles.

423 Comparing this result with the results for ions with  $Z \geq 2$  at  $L > 2.5$  (see Kovtyukh, 2020), one  
424 can conclude that the amplitude of solar-cyclic variations of the radial diffusion coefficient  $D_{LL}$   
425 increases with decreasing  $E$  and  $L$  ( $Z$  is the charge of the atomic nucleus with respect to the charge  
426 of the proton).  
427

428 *Data availability.* All data from this investigation are presented in Figs. 1–5.

429 *Competing interests.* The author declares that there is no conflict of interest.

430 *Acknowledgements.* The author is very grateful to the reviewers for their important and fruitful  
431 comments and proposals regarding the paper and to topical editor, Dr. Elias Roussos, for editing  
432 this paper.

433 *Review statement.* This paper was edited by Elias Roussos and reviewed by two anonymous  
434 referees.

435

436

- 438 Alfvén, H., and Fälthammar, C.-G.: *Cosmical Electrodynamics, Fundamental Principles*,  
 439 Clarendon Press, Oxford, 1963.
- 440 Davis, L. R.: Low energy trapped protons and electrons, *Proc. Plasma Space Sci. Symp.*, Eds. D.  
 441 B. Chang and C. Y. Huang, Washington, P. 212–226, 1965.
- 442 Fennell, J. F., Blake, J. B., and Paulikas, G. A.: Geomagnetically trapped alpha particles, 3. Low-  
 443 altitude outer zone alpha-proton comparisons, *J. Geophys. Res.*, **79**(4), 521–528,  
 444 <https://doi.org/10.1029/JA079i004p00521>, 1974.
- 445 Fischer, H. M., Auschrat, V. W., and Wibberenz, G.: Angular distribution and energy spectra of  
 446 protons of energy  $5 \leq E \leq 50$  MeV in the lower edge of the radiation belt in equatorial latitudes,  
 447 *J. Geophys. Res.*, **82**(4), 537–547, <https://doi.org/10.1029/JA082i004p00537>, 1977.
- 448 Fritz, T. A., and Spjeldvik, W. N.: Steady-state observations of geomagnetically trapped energetic  
 449 heavy ions and their implications for theory, *Planet. Space Sci.*, **29**(11), 1169–1193,  
 450 [https://doi.org/10.1016/0032-0633\(81\)90123-9](https://doi.org/10.1016/0032-0633(81)90123-9), 1981.
- 451 Garcia, H. A., and Spjeldvik, W. N.: Anisotropy characteristics of geomagnetically trapped ions, *J.*  
 452 *Geophys. Res.*, **90**(A1), 359–369, <https://doi.org/10.1029/JA090iA01p00359>, 1985.
- 453 Hoffman, R. A., and Bracken, P. A.: Magnetic effects of the quiet-time proton belt, *J. Geophys.*  
 454 *Res.*, **70**(15), 3541–3556, <https://doi.org/10.1029/JZ070i015p03541>, 1965.
- 455 Ilyin, B. D., Kuznetsov, S. N., Panasyuk, M. I., and Sosnovets, E. N.: Non-adiabatic effects and  
 456 boundary of the trapped protons in the Earth's radiation belts, *Bulletin of the Russian Academy*  
 457 *of Sciences: Physics*, **48**(11), 2200–2203, 1984.
- 458 Kovtyukh, A. S.: Relation between the pitch-angle and energy distributions of ions in the Earth's  
 459 radiation belts, *Geomagn. Aeron.*, **33**(4), 453–460, 1993.
- 460 Kovtyukh, A. S.: Geocorona of hot plasma, *Cosmic Res.*, **39**(6), 527–558,  
 461 <https://doi.org/10.1023/A:1013074126604>, 2001.
- 462 Kovtyukh, A. S.: Radial dependence of ionization losses of protons of the Earth's radiation belts,  
 463 *Ann. Geophys.*, **34**(1), 17–28, <https://doi.org/10.5194/angeo-34-17-2016>, 2016a.
- 464 Kovtyukh, A. S.: Deduction of the rates of radial diffusion of protons from the structure of the  
 465 Earth's radiation belts, *Ann. Geophys.*, **34**(11), 1085–1098, [https://doi.org/10.5194/angeo-34-](https://doi.org/10.5194/angeo-34-1085-2016)  
 466 [1085-2016](https://doi.org/10.5194/angeo-34-1085-2016), 2016b.
- 467 Kovtyukh, A. S.: Ion Composition of the Earth's Radiation Belts in the Range from 100 keV to  
 468 100 MeV/nucleon: Fifty Years of Research, *Space Sci. Rev.*, **214**(8), 124:1–124:30,  
 469 <https://doi.org/10.1007/s11214-018-0560-z>, 2018.
- 470 Kovtyukh, A. S.: Earth's radiation belts' ions: patterns of the spatial-energy structure and its solar-  
 471 cyclic variations, *Ann. Geophys.*, **38**(1), 137–147, [doi:10.5194/angeo-38-137-2020](https://doi.org/10.5194/angeo-38-137-2020), 2020.
- 472 Lejosne, S., and Kollmann, P.: Radiation Belt Radial Diffusion at Earth and Beyond, *Space Sci.*  
 473 *Rev.*, **216**(1), 19:1–19:78, <https://doi.org/10.1007/s11214-020-0642-6>, 2020.
- 474 Leonov, A., Cyamukungu, M., Cabrera, J., Leleux, P., Lemaire, J., Gregorie, G., Benck, S.,  
 475 Mikhailov, V., Bakaldin, A., Galper, A., Koldashov, S., Voronov, S., Casolino, M., De Pascale,  
 476 M., Picozza, P., Sparvolli, R., Ricci, M.: Pitch-angle distribution of trapped energetic protons  
 477 and helium isotop nuclei measured along the Resurs-01 No.4 LEO satellite, *Ann. Geophys.*,  
 478 **23**(8), 2983–2987, <https://doi.org/10.5194/angeo-23-2983-2005>, 2005.
- 479 Northrop, T. G.: *The Adiabatic Motion of Charged Particles*, Wiley-Interscience, NY, USA, 1963.
- 480 Parker, E. N.: Newtonian development of the dynamical properties of ionized gases of low density,  
 481 *Phys. Rev.*, **107**(4), 924–933. <https://doi.org/10.1103/PhysRev.107.924>, 1957.
- 482 Roederer, J. G.: *Dynamics of Geomagnetically Trapped Radiation*, Springer, NY, USA, 1970.
- 483 Sauvaud, J.-A., Walt, M., Delcourt, D., Benoist, C., Penou, E., Chen, Y., and Russell C. T.: Inner  
 484 radiation belt particle acceleration and energy structuring by drift resonance with ULF waves

485 during geomagnetic storms, *J. Geophys. Res. Space Physics*, **118**(4), 1723–1736,  
486 <https://doi.org/10.1002/jgra.50125>, 2013.

487 Selesnick, R. S., Looper, M. D., and Mewaldt, R. A.: A theoretical model of the inner proton  
488 radiation belt, *Space Weather*, **5**(4), S04003, <https://doi.org/10.1029/2006SW000275>, 2007.

489 Selesnick, R. S., Hudson, M. K., and Kress B. T.: Direct observation of the CRAND proton  
490 radiation belt source, *J. Geophys. Res. Space Phys.*, **118**(12), 7532–7537,  
491 <https://doi.org/10.1002/2013JA019338>, 2013.

492 Selesnick, R. S., Baker, D. N., Jaynes, A. N., Li, X., Kanekal, S. G., Hudson, M. K., and Kress, B.  
493 T.: Observations of the inner radiation belt: CRAND and trapped solar protons, *J. Geophys.*  
494 *Res. Space Phys.*, **119**(8), 6541–6552, <https://doi.org/10.1002/2014JA020188>, 2014.

495 Selesnick, R. S., Baker, D. N., Kanekal, S. G., Hoxie, V. C., and Li, X.: Modeling the proton  
496 radiation belt with Van Allen Probes Relativistic Electron-Proton Telescope data, *J. Geophys.*  
497 *Res. Space Phys.*, **123**(1), 685–697, <https://doi.org/10.1002/2017JA024661>, 2018.

498 Shi, R., Summers, D., Ni, B., Manweiler, J. W., Mitchell, D. G., and Lanzerotti, L. J.: A statistical  
499 study of proton pitch-angle distributions measured by the Radiation Belt Storm Probes Ion  
500 Composition Experiment, *J. Geophys. Res. Space Phys.*, **121**(6), 5233–5249,  
501 <https://doi.org/10.1002/2015JA022140>, 2016.

502 Shi, R., Summers, D., Ni, B., Manweiler, J. W., Mitchell, D. G., and Lanzerotti, L. J.: A statistical  
503 study of proton pitch-angle distributions measured by the Radiation Belt Storm Probes Ion  
504 Composition Experiment, *J. Geophys. Res. Space Phys.*, **121**(6), 5233–5249,  
505 <https://doi.org/10.1002/2015JA022140>, 2016.

506 Søråas, F., and Davis, L.R.: Temporal variations of 100 keV to 1700 keV trapped protons observed  
507 on satellite Explorer 26 during first half of 1965, Rep. X-612-68-328, NASA Goddard Space  
508 Flight Cent., Greenbelt, Md., 1968.

509 Williams, D. J., and Lyons, L. R.: The proton ring current and its interaction with plasmopause:  
510 Storm recovery phase, *J. Geophys. Res.*, **79**(28), 4195–4207,  
511 <https://doi.org/10.1029/JA079i028p04195>, 1974.

512 Williams, D. J., and Frank, L. A.: Intense low-energy ion populations at low equatorial altitude, *J.*  
513 *Geophys. Res.*, **89**(A6), 3903–3911, <https://doi.org/10.1029/JA089iA06p03903>, 1984.